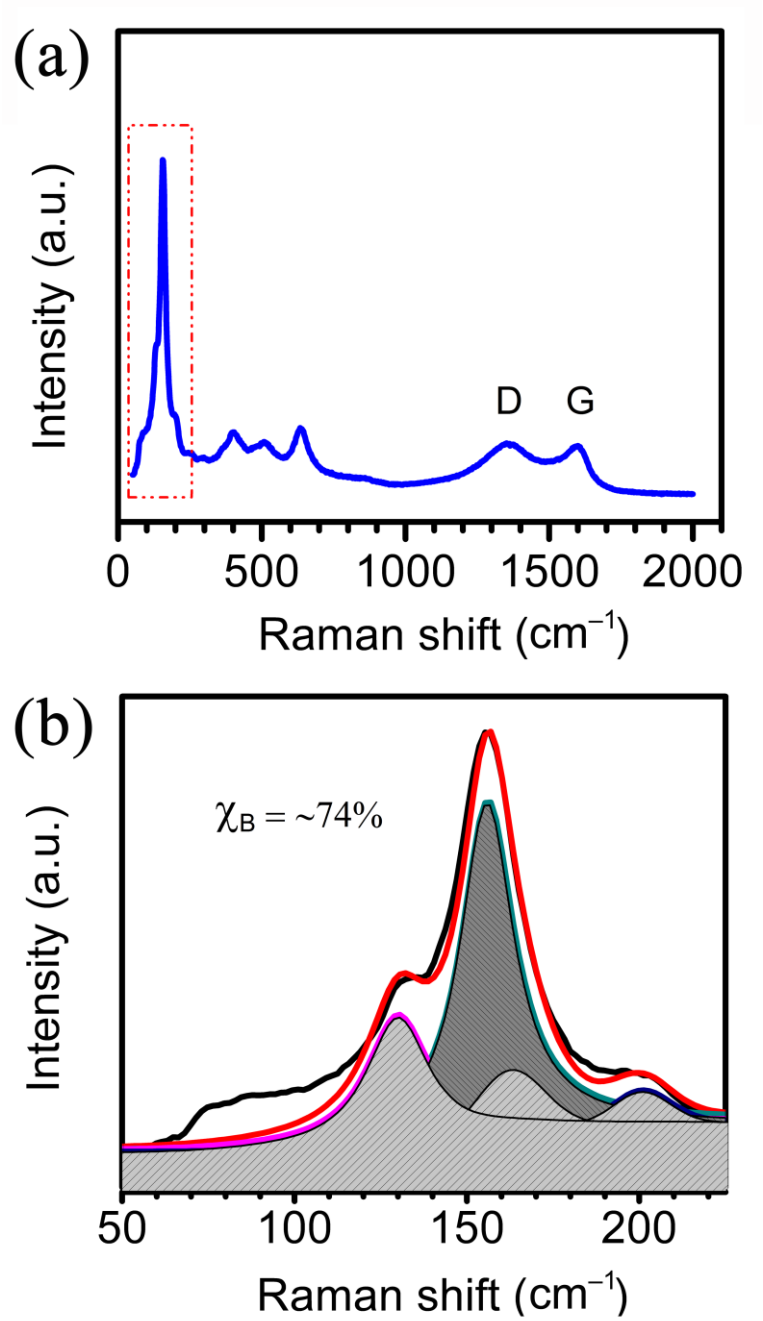

Supplementary Figure 1: Raman spectra of the G-TiO_2 hybrid. (a) Full range Raman spectrum. **(b)** Peak areas assigned to the TiO_2-B (light grey) and anatase (dark grey) phases, respectively. Based on the peak areas, the proportions of the two polytypes can be quantified according to the empirical formula proposed by Brohan[1]: anatase% = $Y/(6.2 - 5.2Y)$, where Y is the value of $S_A/(S_A + S_B)$. The S_A and S_B are the areas of peaks at 152 (main peak of anatase) and 123 cm^{-1} (main peak of TiO_2-B), respectively. Accordingly, the proportion of TiO_2-B phase is valuated to be ca. 74%.

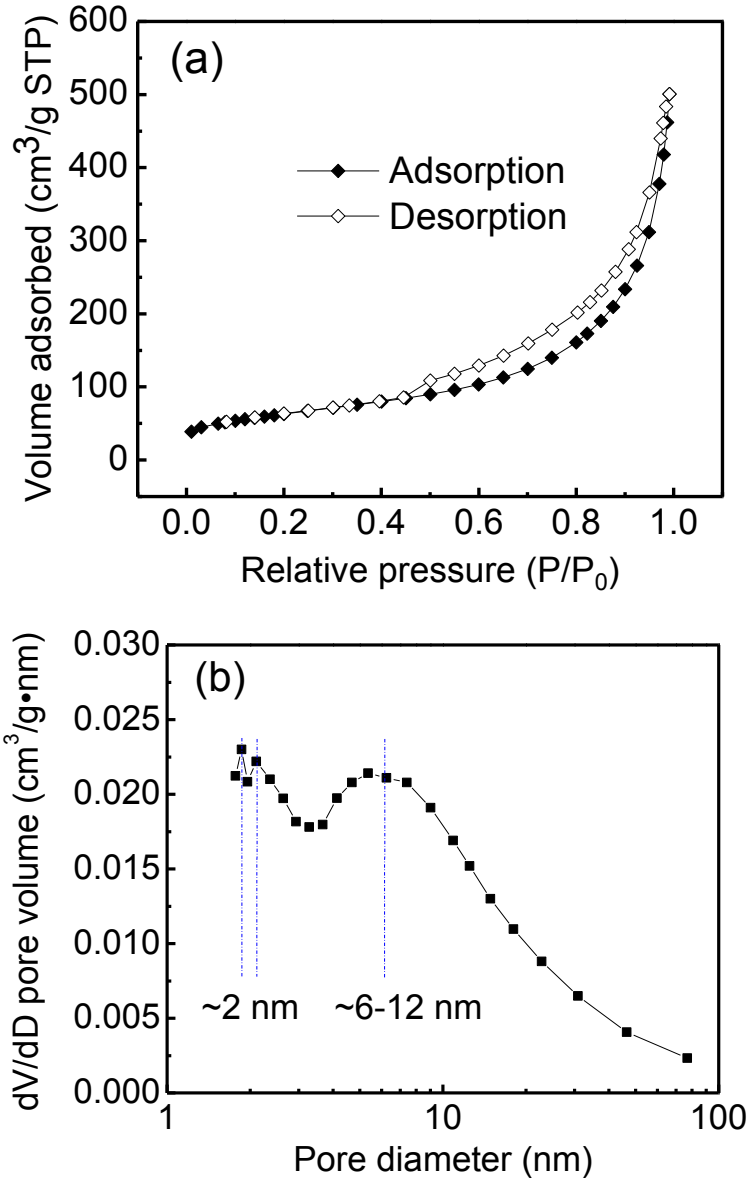

Supplementary Figure 2: Nitrogen adsorption-desorption isotherms (a) and pore size distribution (b) of the G-TiO_2 product. Isotherms show a type-IV behavior with a distinct hysteresis loop in the P/P_0 range of 0.5–1.0, indicating a mesoporous structure of the G-TiO_2 hybrid. The pores with two size ranges co-exist, the smaller is mainly assigned to the nanopores in the graphene sheet originating from heat treatment in air, while the bigger is assigned to the space between the graphene sheets.

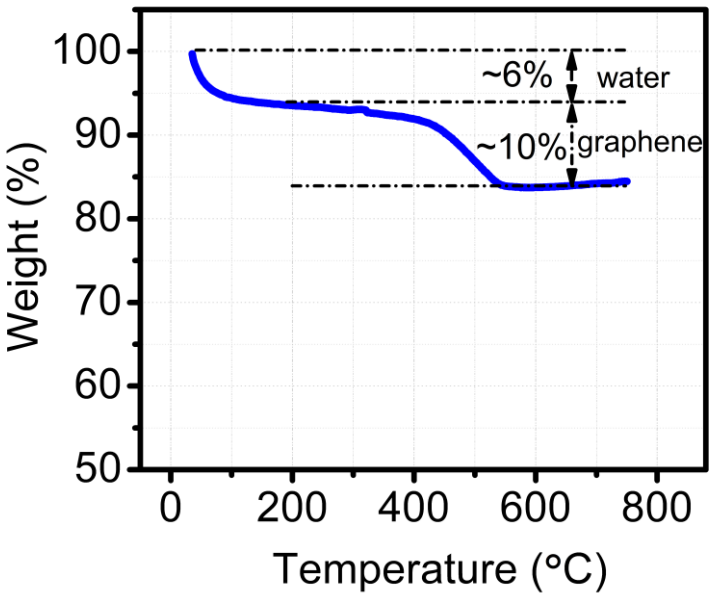

Supplementary Figure 3: Thermogravimetry curve of the G-TiO_2 product. The ~6% weight loss before 200 °C is associated with the evaporation of water, whereas the ~10% weight loss between temperature region of 200–550 °C is assigned to the combustion of graphene in the G-TiO_2 hybrid.

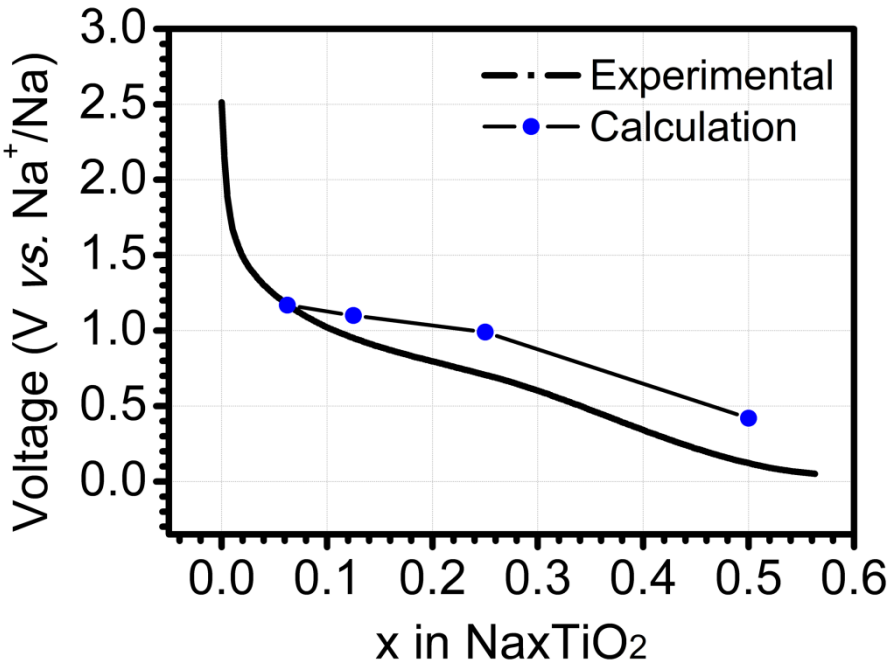

Supplementary Figure 4: Variations of voltages towards different Na concentrations. (a) Experimental results. **(b)** Calculated results. Both of the experimental and calculated voltages show a similar decreasing trend as the Na concentrations increase, resulting in an average voltage of ~0.8 V for the former and ~1.0 V for the latter. The small error between them is rational, considering the integrated influences of polarization, nanostructure, electrolyte and the overbinding of sodium metal and problems with dispersion term in the computations.

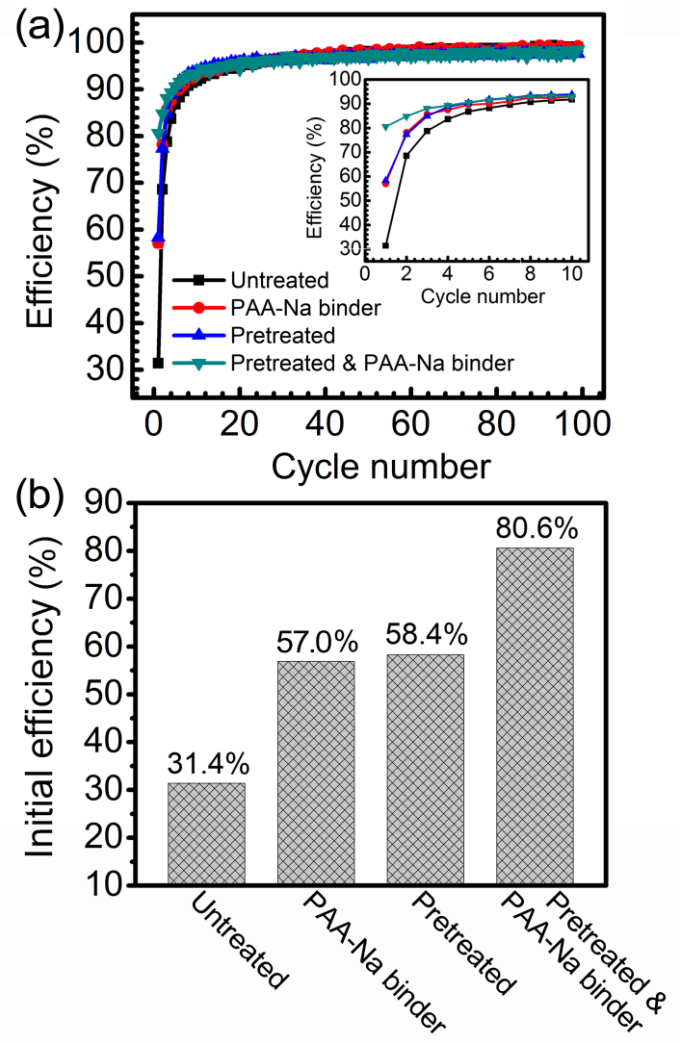

Supplementary Figure 5: Efficiencies of the four G-TiO_2 electrodes with different treatments or/and binders. (a) Efficiencies during 100 cycles. Inset shows the efficiencies for the initial 10 cycles. **(b)** Comparison of the initial efficiencies for the four G-TiO_2 electrodes. From the presented figure, it is observed that significant enhancements in the initial efficiencies can be realized by pretreating the G-TiO_2 hybrid material with butyl lithium or/and using PAA-Na as the binder.

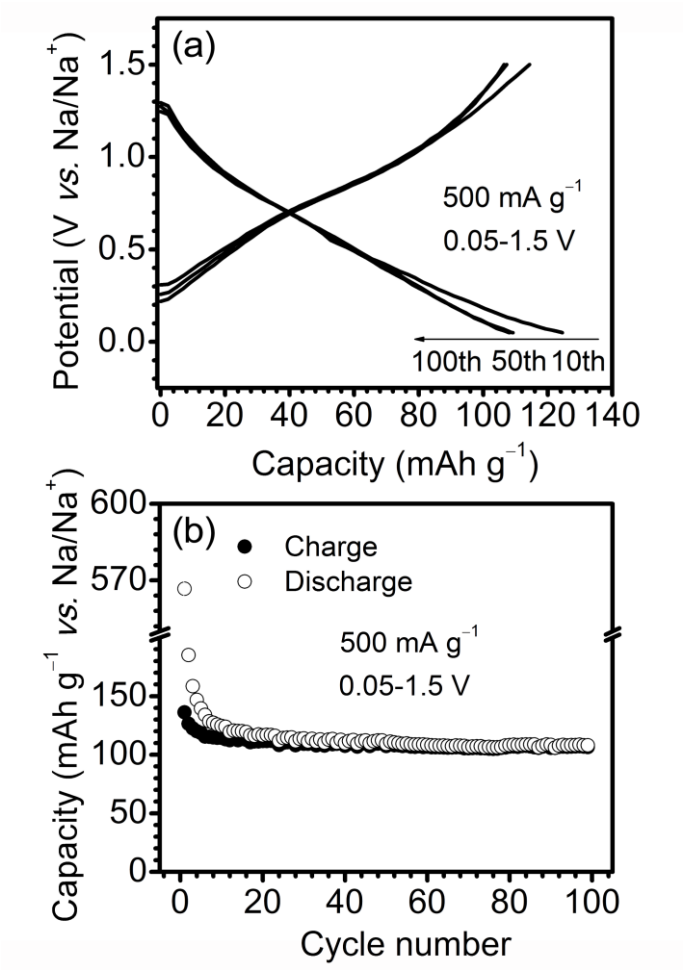

Supplementary Figure 6: Cycling performance of the G-TiO_2 electrode in a potential window of 0.05-1.5 V at 500 mA g^{-1}. (**a**) Charge-discharge curves from selected cycles, the overlaps of the curves in the 50th and 100th cycles demonstrate the high reversibility of the electrode. (**b**) Cycling performance of the electrode, after 50 cycles, the capacities keep almost unchanged.

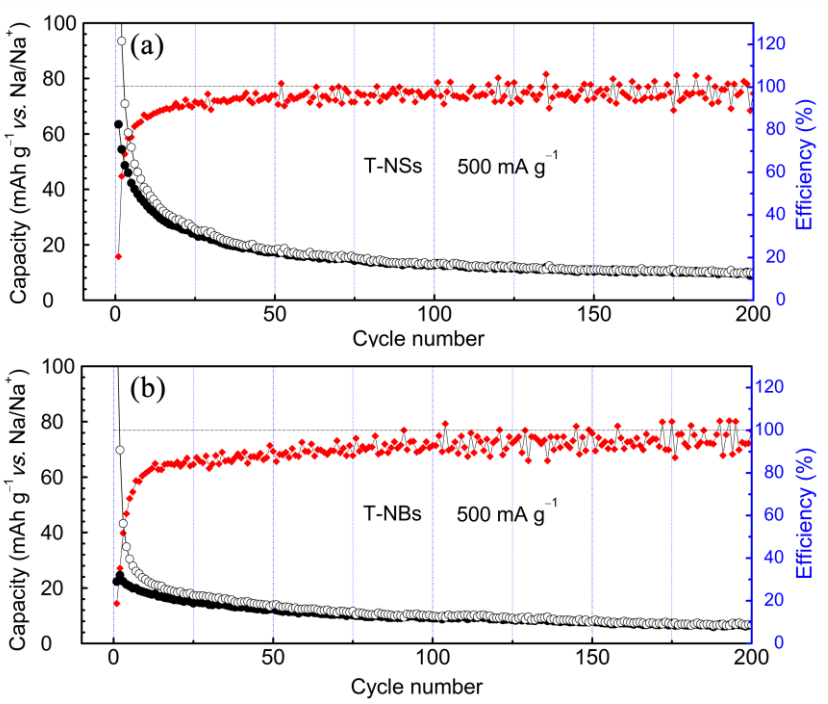

Supplementary Figure 7: Cycling performance of the T-NSs (a) and T-NBs (b) electrodes in the electrolyte of 1 M $NaClO_4$ dissolved in EC and PC (volume ratio 2:1). The inferior sodium storage performances of bare TiO_2 materials are ascribed to the low instinct conductivity for both electron and sodium ions, as well as the difficulty in insertion/extraction of the bigger sodium ions in/out of the host structure.

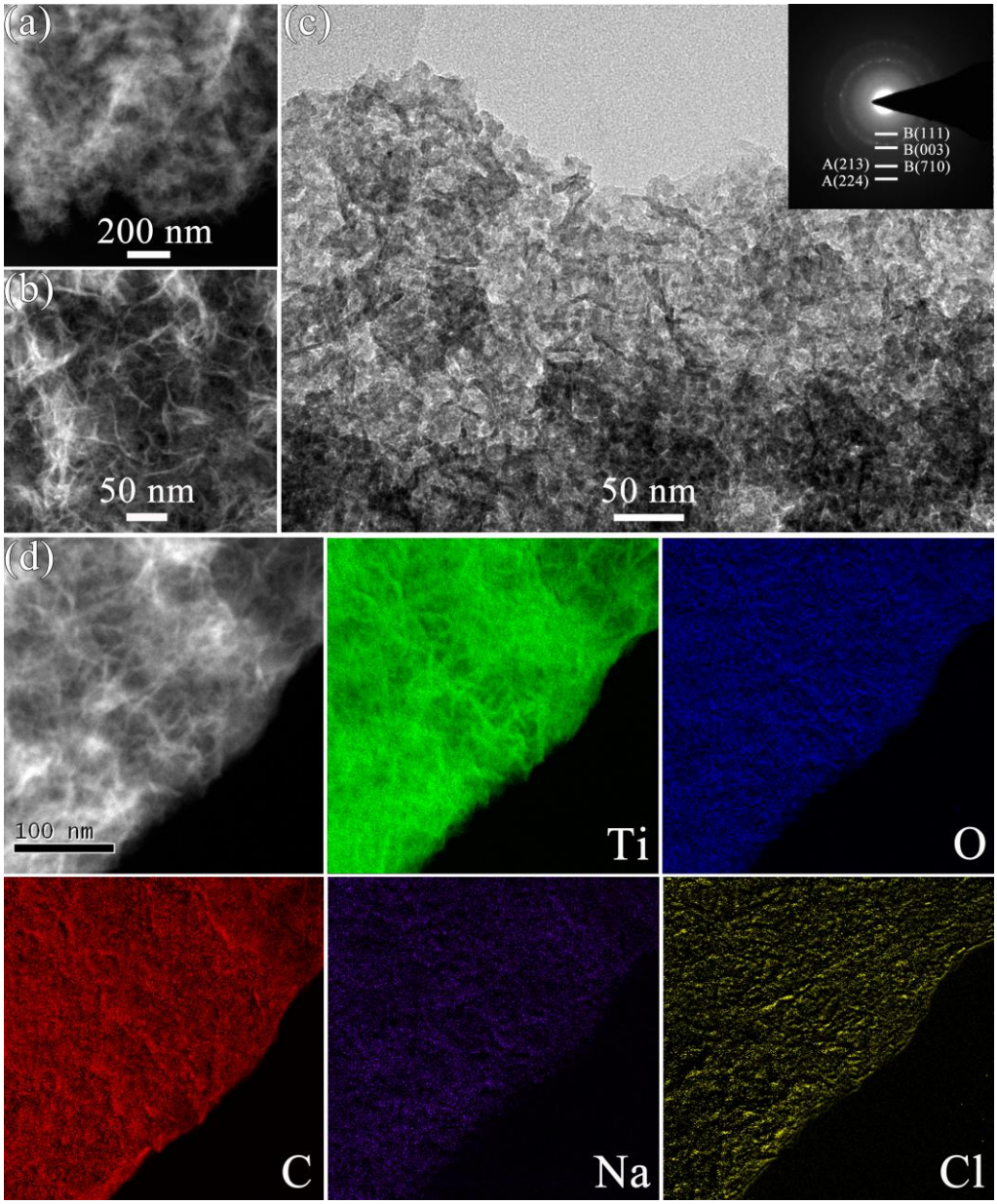

Supplementary Figure 8: Morphology and structure characterization of the G-TiO_2 electrode after 4300 cycles at 500 mA g^{-1} in the electrolyte of 1 M $NaClO_4$ dissolved in EC and PC (volume ratio 2:1). (a,b) High angle annular dark filed (HAADF) STEM images. **(c)** TEM image. Inset shows the corresponding SAED pattern. **(d)** HAADF STEM mapping images of the Ti, O, C, Na and Cl elements. STEM and TEM images indicate the perfect maintenance of the sandwiched sheet on sheet microstructure. Meanwhile, the crystal structure of the G-TiO_2 material is reserved as well, evidenced by the SAED pattern. A well-distribution of Ti, C, O accompanied with Na and Cl elements further confirms the morphology and structure stability of this material.

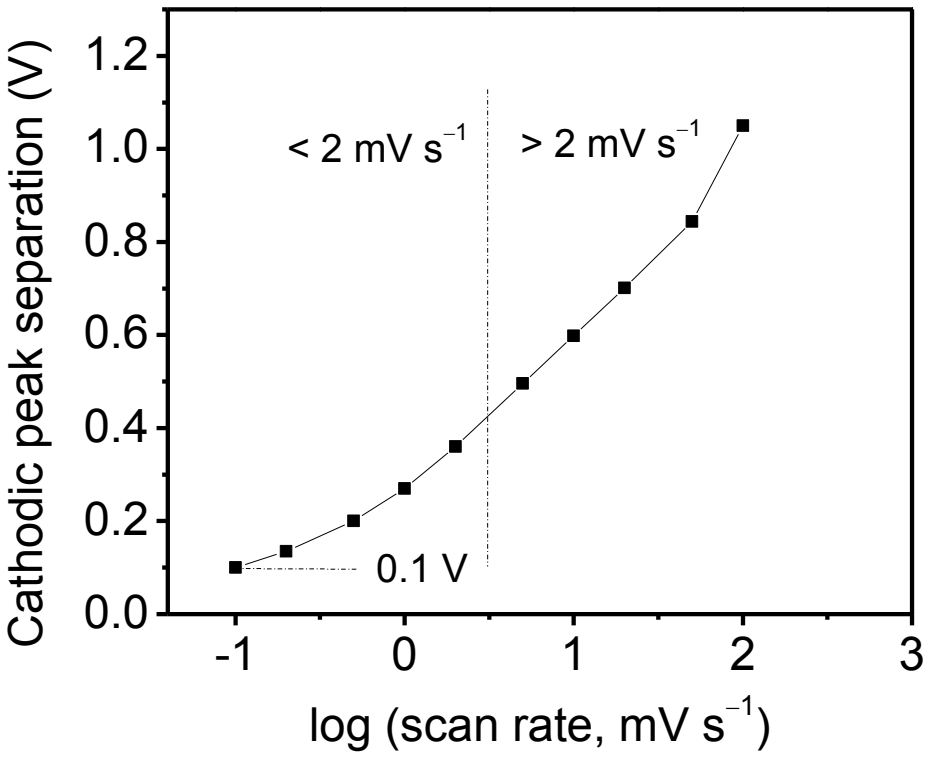

Supplementary Figure 9: Variations of the cathodic peak separation towards the scan rate. The small peak separations at scan rates below 2 mV s^{-1} indicate a low-level polarization in the G-TiO_2 hybrid towards sodium (de)intercalation.

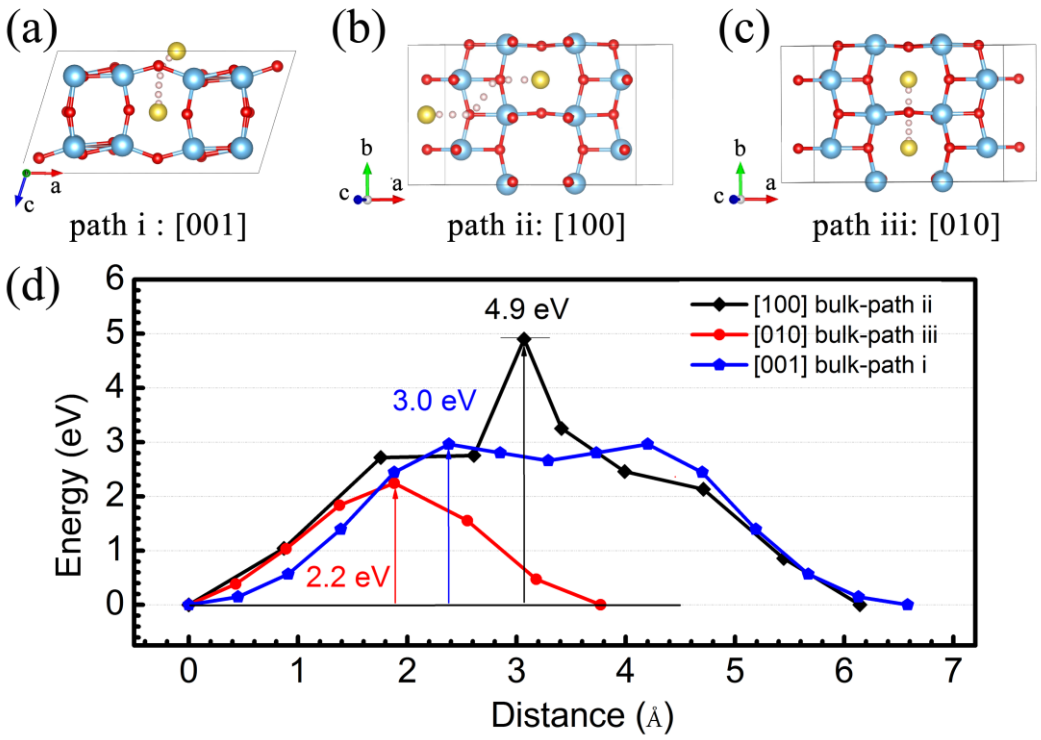

Supplementary Figure 10: Na diffusion in bulk TiO_2-B. (a–c) Illustrations of the Na diffusion paths along the [001], [100] and [010] directions in bulk TiO_2-B material. (**d)** Corresponding migration activation energy of the Na^+ ion calculated with DFT. The three diffusion paths are assigned to path i, migration between the *b*-axis channel through the A1 site along the [001] direction (that is, parallel to the *c*-axis); path ii, migration following a zigzag path within the (001) plane through the A2 site along the [100] direction; path iii, migration through the C site along the [010] direction (along the *b*-axis channel).

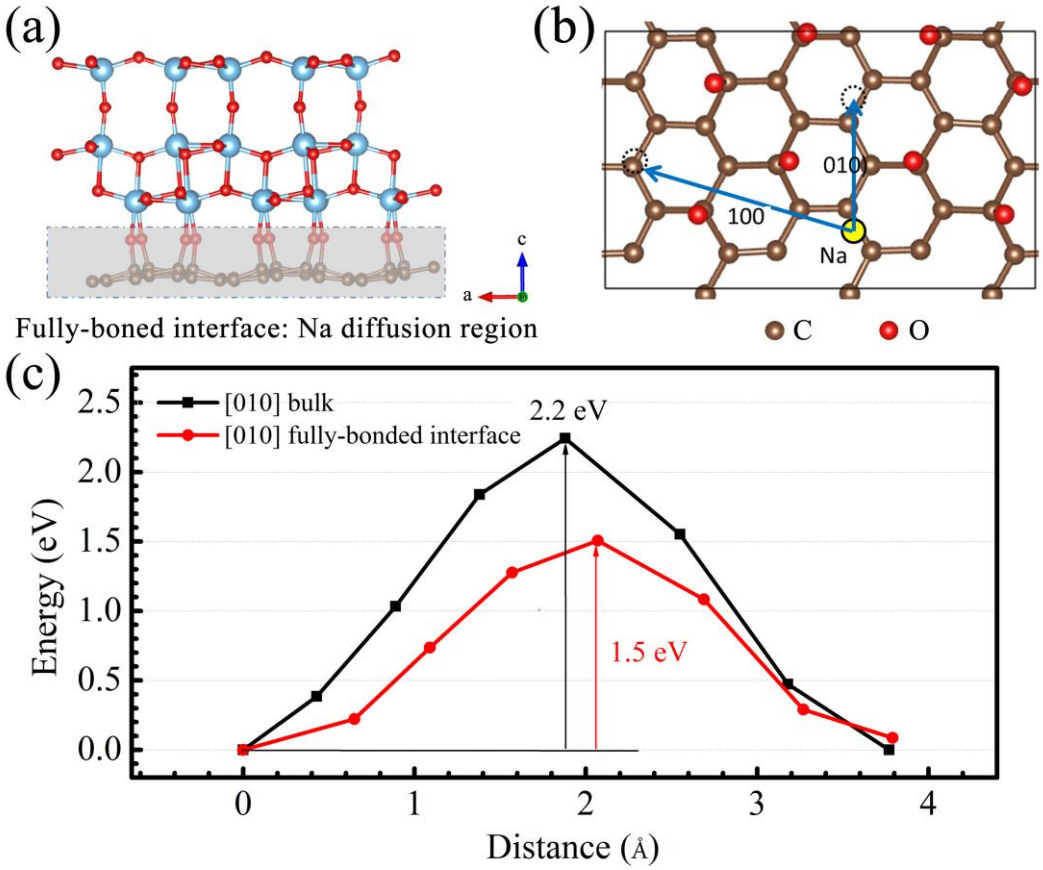

Supplementary Figure 11: Na diffusion in the fully-boned graphene-TiO_2-B (001) interface along the [010] direction. (a) Illustration of the fully-bonded graphene-TiO_2-B (001) interface. (**b)** Top-view of a, illustrating the Na diffusion paths in the interface along the [010] (assigned to path iii') direction. (**c)** Migration activation energy of the Na^+ ion calculated with DFT.

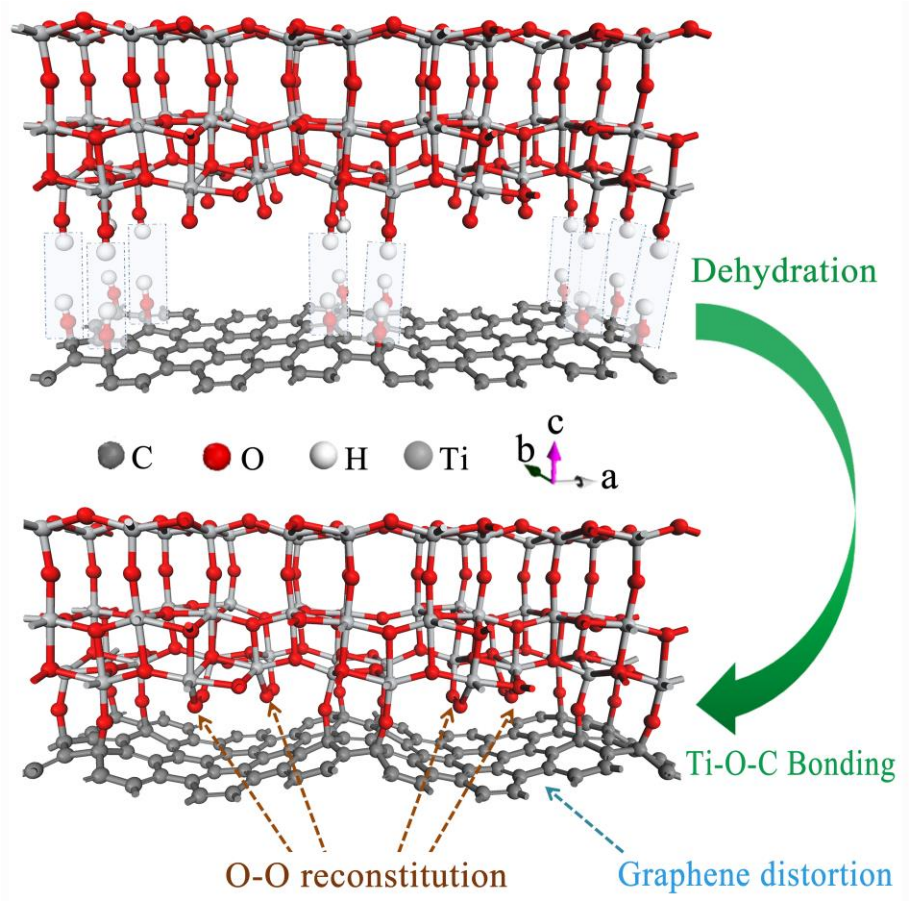

Supplementary Figure 12: Schematic illustration of the possible formation process of the partially-bonded graphene-TiO_2-B (001) interface. The surfaces of the TiO_2 nanocrystalline are known to be covered with –OH groups (Ti–OH)[2]. Generally, the surface oxygen atoms could not be entirely covered due to the relative low concentration of –OH groups. Meanwhile, the –OH groups (C–OH) exist on the graphene surface as well. The surface O_{bulk}–Ti–OH would interact with $C_{graph.}$-OH groups to dehydrate under hydrothermal and/or thermal treatment, leading to the Ti-O-C bond that connects nanocrystalline TiO_2-B and graphene sheets. To reach a lowest total system energy, the dangling O atoms would reconstitute (O_{bulk}–Ti–$O_{surf.}$–$O_{surf.}$–Ti–O_{bulk}) or be passivated by the surface –OH groups (O_{bulk}–Ti–$O_{surf.}$–H), while the graphene sheets are distorted. Consequently, the partially-bonded graphene-TiO_2-B (001) interface is formed.

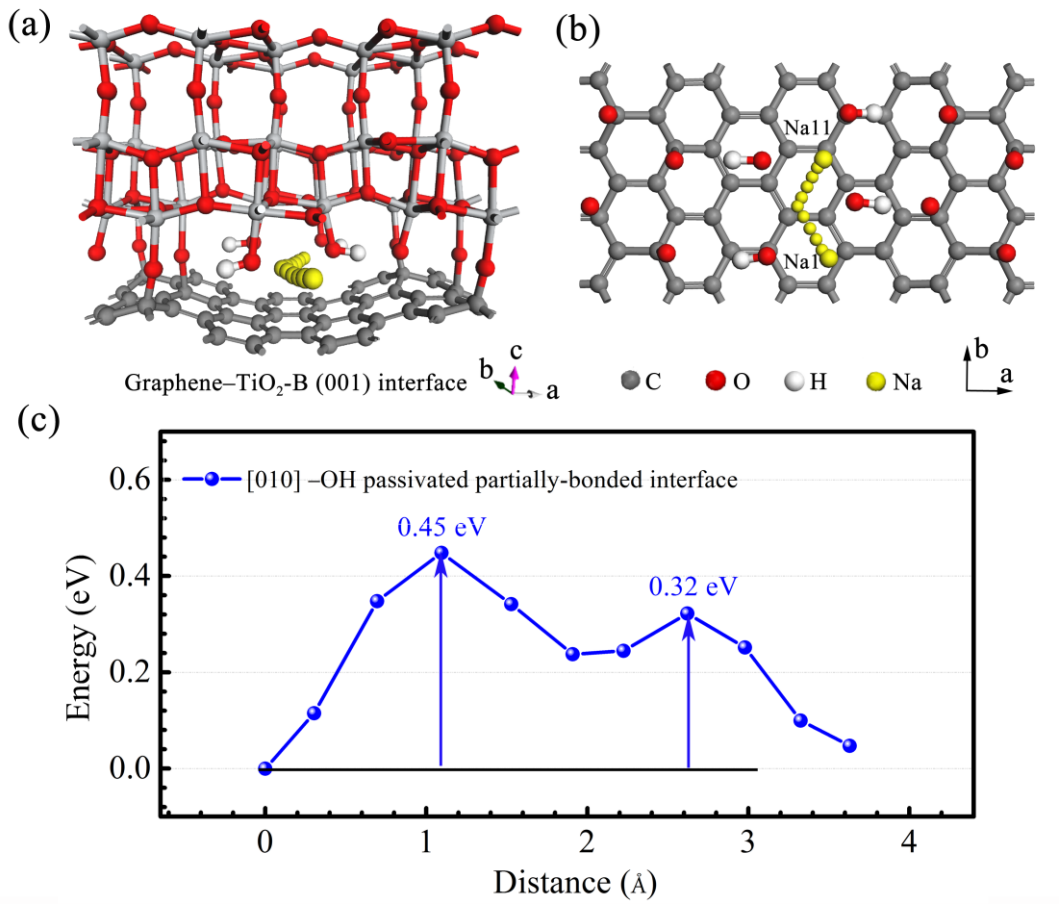

Supplementary Figure 13. Na diffusion in the –OH passivated partially-bonded graphene-TiO_2-B (001) interface. (a) Illustration of the –OH passivated partially-bonded graphene-TiO_2-B (001) interface. **(b)** Top-view of a, illustrating the Na diffusion path along the [010] direction from Na1-Na11 sites. **(c)** Migration activation energy of the Na^+ ion diffusing along the [010] direction in the –OH passivated partially-bonded graphene-TiO_2-B (001) interface calculated with DFT.

Supplementary Table 1: Performances of the G-TiO_2 electrode in sodium cells: effect of binders and pretreatments. Current density = 500 mA h g^{-1}.

Electrode	1st/2nd discharge capacity (mA h g^{-1})	1st efficiency (%)	2nd Capacity retention after 50 cycles (%)
PAA-Na binder	261/199	57.0	64.4
Pretreated with 25% butyl lithium	308/202	58.4	57.0
Pretreated & PAA-Na binder	210/170	80.6	71.2

Supplementary Methods:

The fitting of the X-ray diffraction data:

A Lorentzian peak profile is used to model the size broadening, and the apparent size is assumed to be isotropic by using PO spherical Harmonice (n = 4) with respect to different (hkl) and structure reflections. The dependence of the full width at half maximum, β, on θ is given by $\beta = \lambda/(L_{hkl} \cdot \cos\theta)$, where λ is the wavelength, and L is the refined apparent size parameter. The mixed phases of TiO_2 (B) and anatase were further modeled with the structure films of both through the simulation conditions described above. The phase contents were given by calculating the peak area contents of each phase. The whole-powder-pattern fitting of the in situ diffraction patterns within the 2θ range between 10° and 80° was carried out sequentially in the TOPAS structural refinement package.

Supplementary References:

1. Beuvier, T., Richard-Plouet, M. & Brohan, L. Accurate methods for quantifying the relative ratio of anatase and TiO_2(B) nanoparticles. *J. Phys. Chem. C* **113**, 13703-13706 (2009).
2. Brutti, S., Gentili, V., Menard, H., Scrosati, B. & Bruce, P.G. TiO_2-(B) Nanotubes as Anodes for Lithium Batteries: Origin and Mitigation of Irreversible Capacity. *Adv. Energy Mater.* **2**, 322-327 (2012).